Journal of Innovative Optical Health Sciences
Vol. 13, No. 3 (2020) 2030007 (16 pages)

DOI: 10.1142/S1793545820300074

World Scientific
www.worldscientific.com

Combating acoustic heterogeneity in photoacoustic computed tomography: A review

Tong Wang*, Wen Liu* and Chao Tian†,‡,§
*Department of Optics and Optical Engineering
University of Science and Technology of China Hefei
Anhui 230026, P. R. China

†Department of Precision Machinery and
Precision Instrumentation
University of Science and Technology of China
Hefei, Anhui 230026, P. R. China

‡Key Laboratory of Precision Scientific
Instrumentation of Anhui Higher Education Institutes
University of Science and Technology of China
Hefei, Anhui 230026, P. R. China
§ctian@ustc.edu.cn

Received 11 November 2019
Accepted 16 February 2020
Published 4 March 2020

Based on the energy conversion of light into sound, photoacoustic computed tomography (PACT) is an emerging biomedical imaging modality and has unique applications in a range of biomedical fields. In PACT, image formation relies on a process called acoustic inversion from received photoacoustic signals. While most PACT systems perform this inversion with a basic assumption that biological tissues are acoustically homogeneous, the community gradually realizes that the intrinsic acoustic heterogeneity of tissues could pose distortions and artifacts to finally formed images. This paper surveys the most recent research progress on acoustic heterogeneity correction in PACT. Four major strategies are reviewed in detail, including half-time or partial-time reconstruction, autofocus reconstruction by optimizing sound speed maps, joint reconstruction of optical absorption and sound speed maps, and ultrasound computed tomography (USCT) enhanced reconstruction. The correction of acoustic heterogeneity helps improve the imaging performance of PACT.

Keywords: Photoacoustic computed tomography; image reconstruction; acoustic heterogeneity; ultrasound computed tomography; speed of sound.

§Corresponding author.

1. Introduction

Photoacoustic computed tomography (PACT) is capable of visualizing the optical absorption of biological tissues by combining the excellent contrast in pure optical imaging and high spatial resolution in deep tissues in ultrasound imaging.[1–4] The imaging modality holds great promise for a range of biomedical applications, such as early detection of cancer,[5,6] inflammation evaluation,[7] biopsy guidance,[8,9] retinal imaging,[10] and cellular imaging.[11,12] In PACT, the energy of a laser pulse is absorbed by biological tissues, which will induce a rapid thermal expansion and then excite ultrasound waves. The ultrasound signals travel through the tissue and are detected by ultrasound transducers arranged in a certain detection geometry for final image reconstruction.

Conventional image reconstruction algorithms in PACT are typically based on the assumption that biological tissues are acoustically homogeneous and have a constant speed of sound (SOS) distribution.[13–17] Since the time of flight (TOF) of ultrasound signals directly relates to the position of the target to be reconstructed, it's essential to know the accurate distribution of SOS within the tissues. Currently, the SOS used for PACT image reconstruction is usually selected manually, which is actually different from true values. As a result, distortions and artifacts are common in PA images.

In fact, the tissues in living bodies are typically heterogeneous, violating the aforementioned constant SOS assumption. For example, in transcranial PA imaging, the acoustic reflection and refraction by the skull will cause significant PA signal distortions.[18] Xu *et al.* found that in thermoacoustic tomography of the breast, phase distortions, i.e., TOF errors, are the major source leading to image blurring.[19] Later, Deán-Ben and coworkers investigated the influence of TOF and the corresponding time

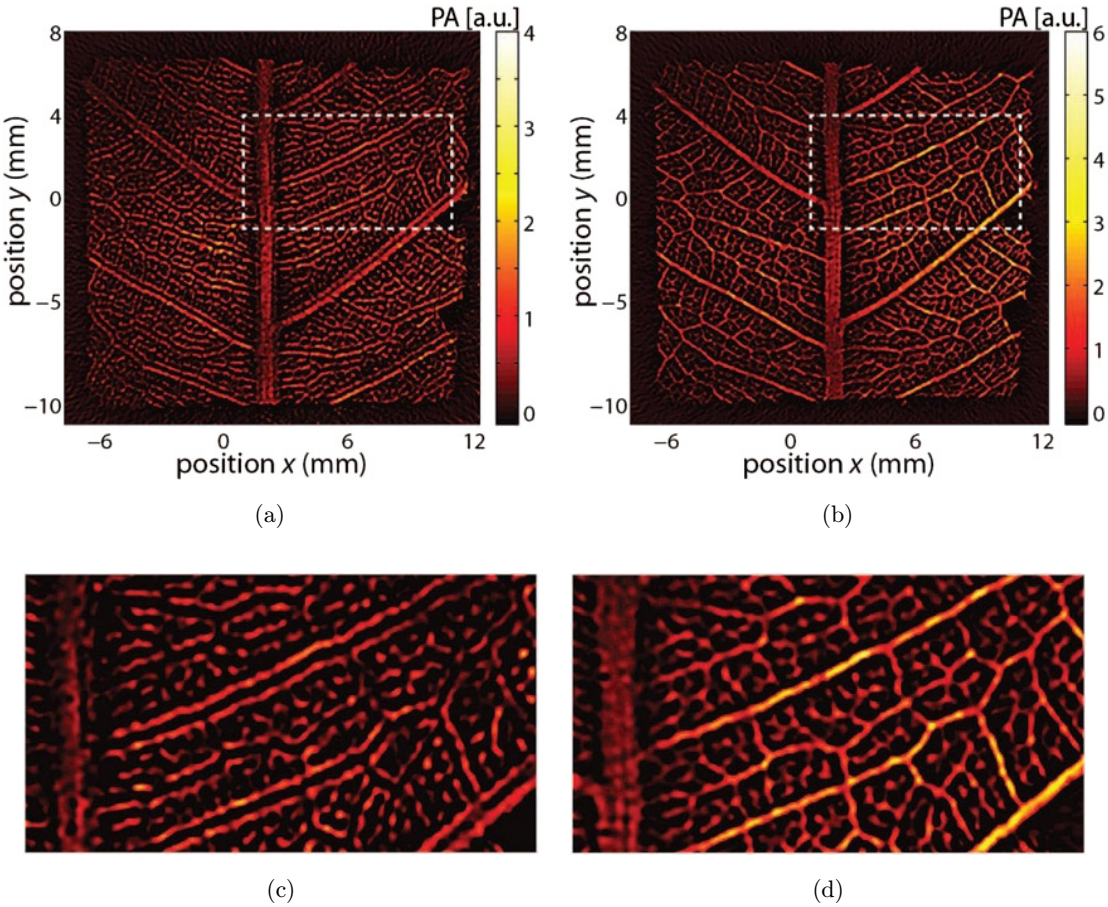

Fig. 1. An example showing how the acoustic heterogeneity may affect the final image quality. (a) PA image of a leaf skeleton reconstructed with a constant SOS of 1506 m/s. (b) PA image of the same leaf skeleton reconstructed with an experimentally measured SOS map. (c) and (d) Corresponding zoomed-in views of the veins in the dashed boxes in (a) and (b). Reproduced with permission from Ref. 22.

shift of wave signals.[20] These efforts theoretically studied the errors induced by spatially varying SOS in PA image reconstruction and show that the SOS pattern used should be sufficiently accurate to produce good imaging results.[21] An example of how acoustic heterogeneity affects the final image quality is shown in Fig. 1.[22] When a constant SOS of 1506 m/s is assumed for image reconstruction, significant double line artifacts [Figs. 1(a) and 1(c)] occurs, which could be significantly mitigated by incorporating measured heterogeneous SOS maps [Figs. 1(b) and 1(d)].

So far, four types of approaches have been proposed to mitigate the artifacts caused by acoustic heterogeneity. They are half-time or partial-time reconstruction,[23,24] autofocus reconstruction,[25–27] joint reconstruction of optical absorption and sound speed maps,[28–30] and ultrasound computed tomography (USCT) enhanced reconstruction,[31–34] as shown in Fig. 2. The half-time or partial-time approaches reconstruct images by eliminating parts of measurement data in the time domain that are distorted by heterogeneous tissues.[23,24] These approaches could achieve better image qualities based on a constant SOS map as compared with conventional reconstruction methods. The autofocus approaches also employ a constant SOS for image reconstruction as half-time methods, but the SOS value is iteratively optimized by evaluating a cost function instead of being guessed based on experience.[25–27] The optimized SOS still deviate from real SOS distributions but may well approximate the overall characteristics of the biological tissue. Different from the previous two methods, the joint reconstruction approaches try to simultaneously extract optical absorption information and SOS distribution from PACT measurement data.[28–30] Since the cost function constructed for optimization is generally not convex, joint reconstruction suffers from the problem of numerical instability. The USCT enhanced reconstruction approaches reconstruct PA images using SOS distribution experimentally measured by USCT and could yield accurate results.[31–34] Compared with the joint

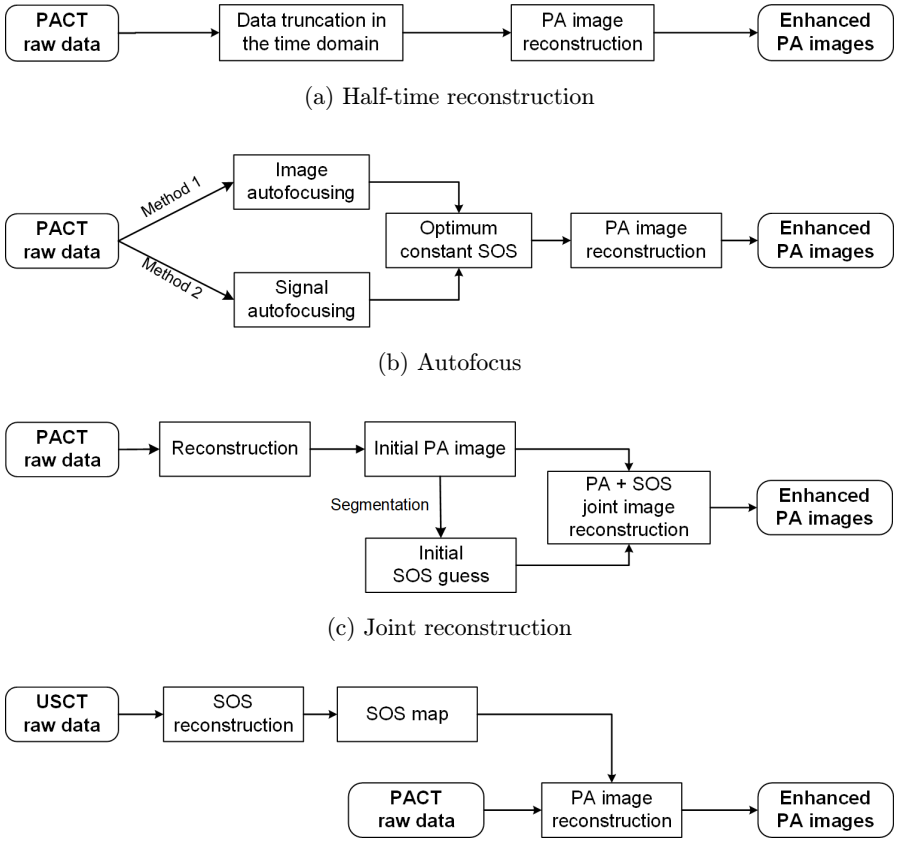

(a) Half-time reconstruction

(b) Autofocus

(c) Joint reconstruction

(d) Two-step reconstruction

Fig. 2. Working procedure of the four methods for mitigating acoustic heterogeneity in PACT.

reconstruction method, the USCT enhanced reconstruction approaches could yield accurate SOS maps and stable PA reconstruction. However, these approaches need extra hardware to measure the SOS map and thus increases system complexity.

In this review, we surveyed the mathematical model describing the acoustic heterogeneity in PACT and state-of-the-art methods to correct acoustic aberrations. The principles and results of the established four approaches are reviewed in detail.

2. Mathematical Model

Considering PACT measurements are performed under the assumption of acoustic homogeneity, biological tissues absorb pulsed laser energy and generate acoustic waves, which are measured by ultrasound transducers located on a detection geometry Ω_0. The measured acoustic pressure at the position $\mathbf{r}_0$ can be expressed as

$$p(\mathbf{r}_0,t)=\frac{\eta}{4\pi}\frac{\partial}{\partial t}\int\frac{A(\mathbf{r})}{|\mathbf{r}_0-\mathbf{r}|}\delta\left(t-\frac{|\mathbf{r}_0-\mathbf{r}|}{v_0}\right)d\mathbf{r}, \quad (1)$$

where $A(\mathbf{r})$ denotes the optical absorption distribution; v_0 is the SOS, which is a constant for homogenous tissues; and η represents a constant coefficient. Introduce a temporal integral function

$$g(\mathbf{r}_0,t)=\frac{4\pi}{\eta}t\int_0^t p(\mathbf{r}_0,t')dt'. \quad (2)$$

Equation (1) can be recast into the integral form as

$$g(\mathbf{r}_0,t)=\int A(\mathbf{r})\frac{1}{v_0}\delta\left(t-\frac{|\mathbf{r}_0-\mathbf{r}|}{v_0}\right)d\mathbf{r}, \quad (3)$$

where $g(\mathbf{r}_0,\ t)$ corresponds to the spherical Radon transform of $A(\mathbf{r})$. Consequently, image reconstruction in PACT can be accomplished by inverting the spherical Radon transform.

Equations (1) and (3) hold only for acoustically homogeneous tissues. For tissues having different acoustic properties, images reconstructed using Eq. (3) will exhibit artifacts and distortions. Taking acoustic heterogeneities into account, Eq. (1) can be generalized as

$$p(\mathbf{r}_0,t)=\frac{\eta}{4\pi}\frac{\partial}{\partial t}\int\frac{A(\mathbf{r})}{|\mathbf{r}_0-\mathbf{r}|}\delta(t-t_f(\mathbf{r},\mathbf{r}_0))d\mathbf{r}, \quad (4)$$

where $t_f(\mathbf{r},\ \mathbf{r}_0)$ is the TOF for ultrasound waves to travel from the point $\mathbf{r}$ within the tissue to the transducer location $\mathbf{r}_0$ and can be mathematically expressed as

$$t_f(\mathbf{r},\mathbf{r}_0)=\int_{\mathbf{r}'\in L(\mathbf{r},\mathbf{r}_0)}\frac{1}{v(\mathbf{r}')}d\mathbf{r}', \quad (5)$$

where $v(\mathbf{r}')$ is the local SOS and $L(\mathbf{r},\ \mathbf{r}_0)$ is the line connecting $\mathbf{r}$ and $\mathbf{r}_0$. When the SOS distribution is uniform, Eq. (4) reduces to Eq. (1). Substituting Eq. (5) into Eq. (2) yields

$$g(\mathbf{r}_0,t)=\int A(\mathbf{r})\frac{t_f(\mathbf{r},\mathbf{r}_0)}{|\mathbf{r}_0-\mathbf{r}|}\delta(t-t_f(\mathbf{r},\mathbf{r}_0))d\mathbf{r}, \quad (6)$$

which is called the generalized Radon transform (GRT) for heterogeneous tissues. When $v(\mathbf{r})=v_0$, the iso-TOF surfaces become spherical, Eq. (6) reduces to Eq. (3).

The eikonal equation is typically adopted to track bent rays in heterogeneous media and has the form as

$$|\nabla t(\mathbf{r})|=\frac{1}{v(\mathbf{r})}, \quad (7)$$

where the gradient of the wavefront $|\nabla t(\mathbf{r})|$ yields a ray vector passing across the wavefront.

3. Sound Speed Correction Strategies

3.1. *Half-time or partial-time reconstruction approaches*

Half-time image reconstruction approaches were first proposed by Anastasio and coworkers in 2005,[23] seeking to exploit redundant information in PACT measurement data. The approaches discard parts of the raw data in the time domain that are disproportionately affected by acoustic heterogeneity and only use unaffected data for image reconstruction. Therefore, it can effectively mitigate image artifacts and distortions.

The raw data $g(\mathbf{r}_0,\ t)$ detected at a location $\mathbf{r}_0$ within the measurement geometry Ω_0 can be separated into two half-time datasets $g_1(\mathbf{r}_0,\ t)$ and $g_2(\mathbf{r}_0,\ t)$ as

$$g_1(\mathbf{r}_0,t)=\begin{cases}g(\mathbf{r}_0,t), & (R_0-R_{\mathrm{ROI}})/v_0\le t\le R_0/v_0,\\ 0, & \text{otherwise},\end{cases} \quad (8)$$

and

$$g_2(\mathbf{r}_0,t)=\begin{cases}g(\mathbf{r}_0,t), & R_0/v_0<t<(R_0+R_{\mathrm{ROI}})/v_0,\\ 0, & \text{otherwise},\end{cases} \quad (9)$$

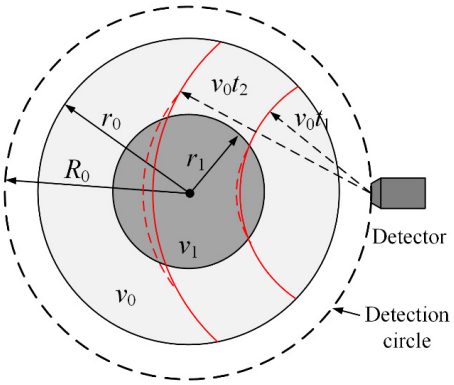

Fig. 3. Schematic showing heterogeneous sound speed distribution. Modified version of Fig. 3 in Ref. 23.

where R_0 is the radius of the measurement sphere enclosed by the detector and R_{ROI} is the radius of the region of interest. For homogenous media with a constant SOS, the data function is truncated at the time point $t_{\mathrm{half}} = t_{\mathrm{full}}/2$. For circular and spherical measurement geometries, $t_{\mathrm{half}} = R_0/v_0$.

Figure 3 is a two-dimensional example illustrating why the half-time reconstruction approaches could mitigate image artifacts and distortions in cases of acoustic heterogeneities. The SOS map contains two concentric regions with different radii (inner disk: r_1, outer ring: r_0) and sound speeds (inner disk: v_1, outer ring: v_0, and $v_1 \neq v_0$). The measurement geometry is a circle with a radius of R_0. The solid and dashed arc contours in red show constant acoustic path lengths to the detector for homogenous SOS map ($v_1 = v_0$) and heterogeneous SOS map ($v_1 > v_0$), respectively. Obviously, the difference between the solid and dashed arc contours is caused by the mismatch of SOS in the two regions and it will become more severe as the propagation time t increases. Specifically, when $v_0t_1 < R_0$–r_1, the heterogeneity will not impact the detected signals and the data function $g_1(\mathbf{r}_0, t)$ is much less affected by acoustic heterogeneities than $g_2(\mathbf{r}_0, t)$ and $g(\mathbf{r}_0, t)$.

Figure 4 shows a group of simulations comparing images reconstructed by full-time and half-time approaches. The predefined SOS ratios v_1/v_0 in the two regions for Figs. 4(a)–4(c) are 0.9, 1.07, and 1.12, respectively. The subfigures on the left column were reconstructed using half-time raw data while those on the right were reconstructed using full-time raw data. Half-time reconstruction results have fewer artifacts and distortions compared with those reconstructed by full-time approaches.

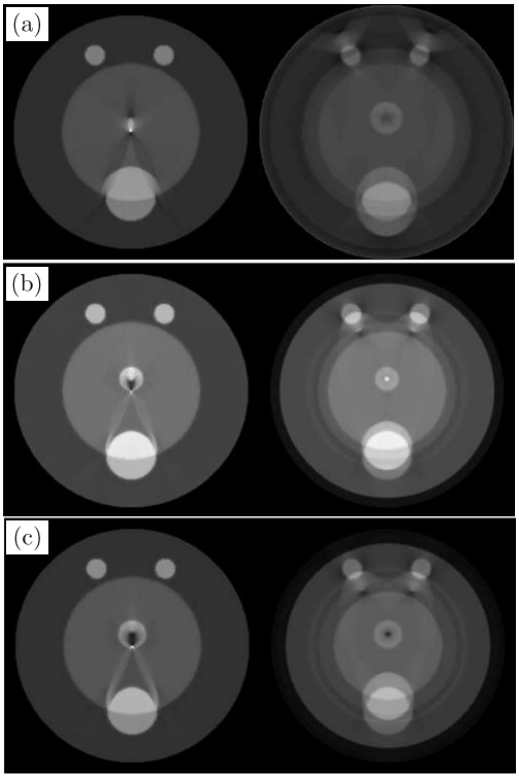

Fig. 4. Images reconstructed from simulated thermoacoustic tomography measurement data containing the effects of acoustic heterogeneities. The images in subfigures (a), (b), and (c) were reconstructed from data corresponding to acoustic speed map with $v_1/v_0 = 0.9$, 1.07, and 1.12, respectively. The images in the left and right panels of each subfigure were reconstructed from half- and full-time datasets, respectively. Reproduced with permission from Ref. 23.

The half-time reconstruction approaches show improved performance compared to conventional full-time reconstruction methods and were generalized to a partial-time reconstruction approach by Poudel and coworkers.[24] In contrast to half-time approaches using temporally halved raw data, the partial-time method truncates raw data according to the locations of the isolated heterogeneous region and ultrasound detectors. It has better performance when the approximate sizes and locations of isolated heterogeneous structures, such as bones or gas pockets, are known.

3.2. *Autofocus approaches*

In PA image reconstruction, the selection of the SOS of the tissue is critical to the final image quality. Typically, the SOS used for image reconstruction is empirically chosen as a constant value (e.g., 1540 m/s), which may cause blurring to finally

reconstructed images.[26,27] To solve this problem, autofocus methods have been proposed to optimally select the SOS for image reconstruction. These methods aim at automatically choosing the optimum SOS that can yield the best reconstruction results. The autofocus approaches usually first determine the optimum SOS by optimizing a focusing function and then reconstruct PA images based on the optimum SOS. Based on how the focusing function is constructed, autofocus approaches can be divided into image autofocus methods and signal autofocus methods.

3.2.1. *Image autofocus*

In practice, the SOS used for image reconstruction is manually tuned to maximize the sharpness of prominent image features, especially when the images contain vascular features. A sharper image usually contains more high-frequency components than its blurry counterparts.

Such a procedure can be automatically performed with an autofocus method,[25] which selects the optimal SOS to maximize the sharpness of reconstructed PA images.[35] The methods of using SOS as a focusing parameter have been used in many other modalities, such as microscopy,[36] optical coherence tomography,[37] and computed tomography.[38] In this method, three focusing functions, that is, the Brenner gradient, the Tenenbaum gradient, and the normalized variance, can be used to autofocus the images. The Brenner gradient computes the difference between a pixel value and its neighbors two points away and can be written as

$$F_{\text{Brenner}} = \sum_{x,y} (f_{x+2,y} - f_{x,y})^2 + (f_{x,y+2} - f_{x,y})^2, \quad (10)$$

where $f_{x,y} = f(x, y)$ is the gray-level intensity of the pixel at (x, y) in the image. The Tenenbaum gradient makes use of the Sobel operators and can be written as

$$F_{\text{Tenenbaum}} = \sum_{x,y} (\omega * f_{x,y})^2 + (\omega^T * f_{x,y})^2, \quad (11)$$

where ω is the Sobel operator and * denotes two-dimensional convolution. The normalized variance quantifies variations of pixel values and can be written as

$$F_{\text{variance}} = \frac{1}{\mu} \sum_{x,y} (f_{x,y} - \mu)^2, \quad (12)$$

where μ is the mean pixel value. The SOS is regarded as optimal when the corresponding autofocus functions reach their maxima.

These focusing functions can be used as sharpness metrics and the SOS is automatically updated until the maximum is reached. The performance of the three cost functions was evaluated by a phantom experiment shown in Fig. 5. The result shows that the three focusing functions reach the maximum at a common SOS, where the reconstructed images have the maximum sharpness.

The autofocus functions are not necessarily limited to the functions listed here and can be of other types. Mandal *et al.* tested several different autofocus functions and classified them into three major groups, that is, intensity-based, gradient-based and edge-based measures.[39] The intensity-based metrics measure the maximum pixel intensity or the maximum intensity range of the images, which is intuitive but is artifact-prone if noise or artifacts yield similar high-intensity features. The Brenner's gradient and Tenenbaum's gradient belong to the

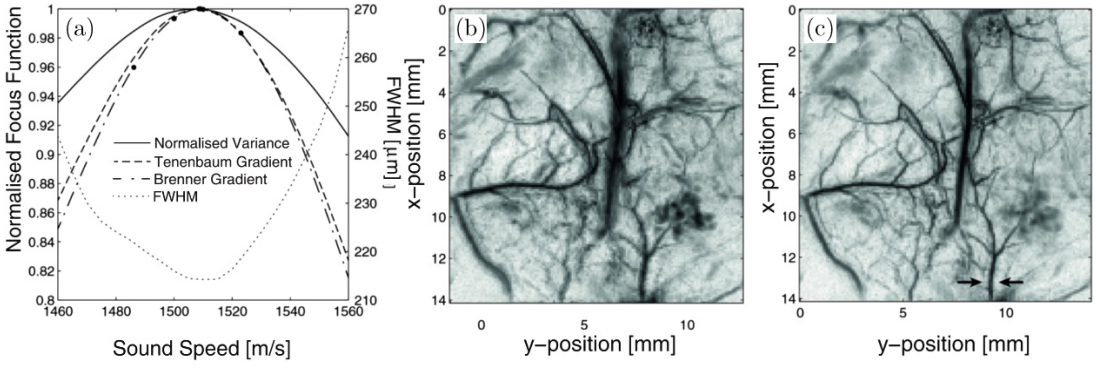

Fig. 5. Image enhancement by the autofocus method. (a) Three investigated focus metrics give the same value for the optimum SOS. (b) Defocused image reconstructed using an SOS overestimated by 5%. (c) Focused image reconstructed using the optimized SOS. Reproduced with permission from Ref. 25.

gradient-based measures and the normalized variance can be classified into the edge-based measures. Mandal *et al.* found that the edge-based measures have the best performance.[39]

This image sharpness maximization method can robustly determine the optimum SOS and highlights dominant image features. However, it cannot distinguish artifacts from real image details, which means that it may incorrectly maximize the sharpness of the artifacts.

3.2.2. *Signal autofocus*

In addition to image autofocus, Yoon *et al.* proposed a signal autofocus method which can also determine the optimal SOS.[26] In this method, the optimal SOS is determined by maximizing a coherence factor to best focus PA signals (Fig. 6). The coherence factor used as a focusing function is computed from delay-compensated PA data as

$$F_l(t) = \frac{1}{N} \frac{\left| \sum_{n=0}^{N-1} x_{l,n}(t - \tau_n) \right|^2}{\sum_{n=0}^{N-1} |x_{l,n}(t - \tau_n)|^2}, \quad (13)$$

where N is the number of channels, τ_n is the time delay for the nth element located at (x_n, z_n), and $x_{l,n}(t)$ is the signal received by the nth element for the lth scanline. Optimal SOS is determined when the coherence factor function reaches its maximum, i.e.,

$$v_{\text{optimum}} = \arg\max_{v} [CF_l(t)]. \quad (14)$$

Another focusing function that can be used to evaluate the optimum SOS is proposed by Cong *et al.* and can be written as[27]

$$F(x; v) = \frac{1}{N} \sum_{z=1}^{Z} \sum_{n=1}^{N} |p_n(x, z; v) - \mu(x, z; v)|, \quad (15)$$

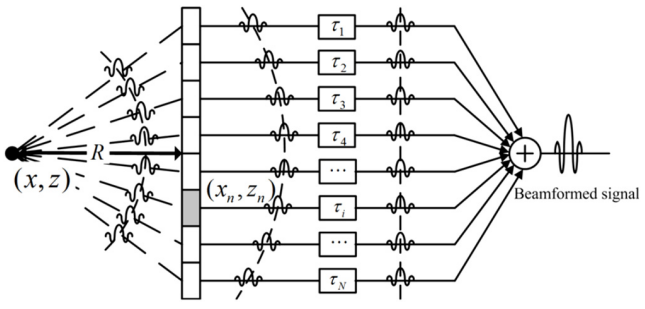

Fig. 6. Schematic showing that PA signals generated from a point-like absorber are received by a detector array when the assumed sound speed is equal to the true one. Reproduced with permission from Ref. 26.

where Z is the number of focal points per scanline in the ROI, N is the number of sensor elements, p_n is the focused PA signal with a sound speed v for the zth focal point at the xth scanline, μ is the mean value of the focused PA signals. When the SOS used for beamforming is equal or close enough to the true value, the beamformed signals are in phase and the focusing function reaches its minimum.

Since image autofocus and signal autofocus both need focusing functions associated with the SOS, they fundamentally work in a similar way and can both improve the image quality by optimizing the SOS. However, since the SOS distributions within biological tissues are usually heterogeneous, the enhancement achieved by the autofocus approaches is limited especially in the case of strong SOS variations. More sophisticated approaches are required to retrieve the SOS distribution for better compensation for the acoustic heterogeneity.

3.3. *Joint reconstruction approaches*

Knowledge of SOS distribution of the tissues can help mitigate imaging artifacts but is difficult to obtain. Multiple methods have been developed to simultaneously reconstruct the SOS and optical absorption distributions with only PACT measurements.[40,41] One algorithm that solves a Helmholtz-like PA wave equation using a finite element method (FEM) was proposed by Jiang *et al.* and Yuan *et al.* and validated with numerical simulations and phantom experiments.[42,43] By introducing the FEM method to solve an accurate imaging model, this approach has better accuracy but suffers from the problem of slow computation. This FEM-based algorithm could also be extended to three-dimensional cases.[44] In addition, several other algorithms were also proposed such as the TR adjoint method,[45] the Radon transforms and Fourier transforms based method,[40,41] and the Born approximation-based method.[46] While most of the methods were only validated by numerical simulations and phantom experiments, a few were demonstrated through *in vivo* experiments and will be described with greater details.

3.3.1. *Feature coupling based joint reconstruction*

The feature coupling method was proposed by Cai and coworkers for joint reconstruction of the SOS

distribution and enhancement of PA images with PA measurements using a full ring transducer array PACT system.[30] This method is based on the fact that, for tissues with heterogeneous SOS distribution, any subsets of a full ring transducer array produce images with displaced features. The similarities of these images can be maximized to update the SOS distribution.

In this method, the SOS map is segmented into multiple regions with different SOS values, denoted as $\mathbf{v} = [v_1, v_2, \ldots, v_n]$. The initial segmentation of the SOS map is achieved based on the PA image reconstructed by the half-time back-projection method[23] using a predefined constant SOS. Full ring PA data are split into two parts, each part is used separately to reconstruct PA images. The features of these two images are different because the SOS maps derivate from real distributions. The similarity of the two images reconstructed by two half-ring data is maximized to get the best SOS map, i.e.,

$$\mathbf{v} = \arg\max_{\mathbf{v}}[c(\mathbf{v})], \tag{16}$$

where c is the correlation coefficient measuring the similarity of two images and can be written as

$$c(\mathbf{v}) = f_1(\Theta) \star f_2(\Theta), \tag{17}$$

where f_1 and f_2 are reconstructed half-ring images, $\star$ denotes correlation, and Θ means the target region in the images used to evaluate the correlation coefficient.

The performance of this method has been demonstrated by *in vivo* experiments shown in Fig. 7. The results highlighted in the red box show that the feature coupling method can mitigate image distortions and blurring and have a better performance than the popular half-time back projection algorithm.

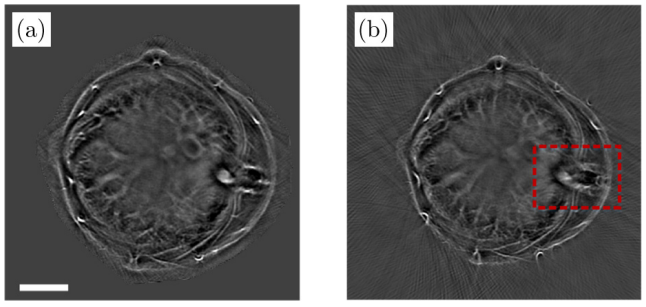

Fig. 7. PA images of a mouse liver reconstructed by the feature coupling method (a) and the half-time back projection method (b). The image in (a) has no splitting artifacts, which are present in (b). Scale bar: 5 mm. Reproduced with permission from Ref. 30.

The concept of feature coupling is generic and can be applied to other detection geometries, but the detection surface division strategy should be adjusted accordingly. It should be noted that the feature coupling method optimizes the SOS distribution iteratively by maximizing the similarity measure, and therefore, a good initial guess of the SOS distribution is essential for the efficiency. In addition, if large structures with distinct features are present in the images, the performance of the feature coupling method may drop dramatically.

3.3.2. *Regularization based joint reconstruction*

Zhang and Anastasio reported a heuristic method to simultaneously reconstruct the SOS distribution, $v(\mathbf{r})$, and the optical absorption distribution, $A(\mathbf{r})$, from PACT measurements.[28] The two distributions are alternatively reconstructed in an iteration process, where the optical absorption map is recovered by the full-wave iterative method[47] and the SOS map is reconstructed by the use of a nonlinear optimization algorithm based on the Fréchet derivative of an objective function with respect to $v(\mathbf{r})$.[48,49]

In this method, the distribution of SOS is unknown and is parameterized. To reconstruct $A(\mathbf{r})$ and $v(\mathbf{r})$ simultaneously, two-fold data redundancy is adopted.[23,50] Each of the two half-time dataset contains complete information of the optical absorption map and can be used to reconstruct PA images. With complete knowledge of the SOS distribution, these two results should be the same. However, in the case of data inconsistencies, this is untrue and their differences should be minimized based on the SOS distribution. As such, both $A(\mathbf{r})$ and $v(\mathbf{r})$ can be recovered iteratively.

The generalized imaging model in Eq. (6) can be written in the operator form as

$$g(\mathbf{r}_0, t) = G(v)A(\mathbf{r}), \tag{18}$$

where $G(v)$ represents the generalized Radon transform operator. The estimation process of the SOS, $v(\mathbf{r})$, and the optical absorption, $A(\mathbf{r})$, is achieved using the following formulas:

$$\Phi(v, A) = \|g - GA\|^2 + \beta_1 P_1(v) + \beta_2 P_2(A), \tag{19}$$

$$v^*, A^* = \operatorname*{argmin}_{v,A} \Phi(v, A), \tag{20}$$

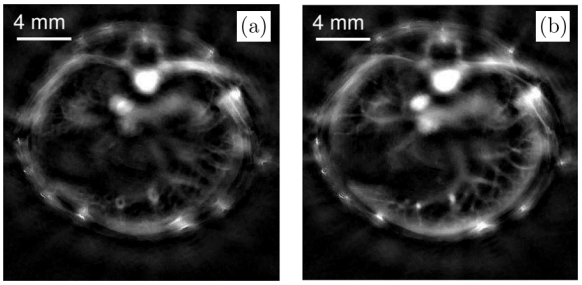

Fig. 8. Parameterized joint reconstruction. Initial pressure distributions reconstructed with a constant SOS of 1500 m/s (a) and the SOS distribution obtained by parameterized joint reconstruction (b). Reproduced with permission from Ref. 29.

where $P_1(v)$ and $P_2(A)$ are penalty terms that regularize the smoothness of the solutions and β_1 and β_2 are weighting factors.

By alternately fixing v or A and update the other one, both distributions can be simultaneously reconstructed. Based on this model, Shan *et al.* proposed a deep-learning approach in 2019 using a simultaneous reconstruction network (SR-Net) to update the initial pressure and the SOS for each iteration.[51] *In vivo* experiments (Fig. 8) demonstrates the performance of a more advanced joint reconstruction method called parameterized joint reconstruction.[29]

The numerical stability of this joint reconstruction method was studied by Huang *et al.*[52] Since this method estimates two distributions alternatively, the errors induced in one step will affect the reconstruction accuracy in the next step, which means that errors will accumulate during the iteration process. In addition, the problem of reconstructing the SOS map, v, from estimated optical absorption map, A, is ill-conditioned, and a small fluctuation of A may cause significant variations of the reconstructed v.[53] *Prior* information or knowledge is often incorporated in the mathematical model to stabilize the numerical process; for instance, the distributions of $A(\mathbf{r})$ and $v(\mathbf{r})$ may have some constraints,[54] and the detection surface may have specific geometrical shapes.[40]

This method is of significance since the results are much better than that based on a constant SOS assumption. Moreover, extra information such as USCT measurement data can be used to improve numerical stability.[55]

3.4. *USCT-enhanced reconstruction approaches*

Another strategy is to independently reconstruct the SOS map and the optical absorption distribution by USCT and PACT, respectively. Using USCT setups, high-resolution SOS maps can be recovered, which can then be used to enhance the reconstruction of optical absorption maps. There are several algorithms focusing on PA reconstruction problems in acoustic heterogeneous media, including the time reversal,[56–58] the iterative full-wave inversion,[47,59] the Neumann-series or iterative time reversal approach,[60,61] the GRT,[62,63] and the statistical methods.[64] These reconstruction methods need measured acoustic heterogeneity as input to accurately reconstruct PA images. Some researchers try to avoid this restriction. For example, Zhang *et al.* proposed a method using correlation information between thermoacoustic signals to compensate for acoustic heterogeneity.[65] This method compensates for travel time perturbation of thermoacoustic signals detected at locations symmetric to the origin and then reconstructs the optical absorption map. The TOF value is directly calculated from PACT signals instead of measured SOS maps.

The most difficult and critical part of USCT-enhance reconstruction approaches is how to implement the two different measurement procedures at the same time. Since USCT and PACT both detect ultrasound signals, these two measurement systems can share the same set of detectors. Efforts have been made to set up imaging systems capable of both USCT and PACT imaging. Jin and Wang integrated USCT measurements into a thermoacoustic tomography setup by adding an opposite-facing ultrasound transmitter, as shown in Fig. 9.[31] In the USCT process, the transmitter and receiver work together to obtain scan data and get the SOS map of the sample. In the thermoacoustic tomography process, the sample absorbs microwave energy and generates ultrasound waves, which are detected by a receiver to reconstructed energy absorption distribution.

Manohar *et al.* proposed a similar design to achieve this purpose.[32] However, instead of using an ultrasound transducer as an active transmitter, they used passive elements, i.e., carbon fiber illuminated by nanosecond laser pulses, to generate ultrasound waves for USCT measurements. This idea of leveraging laser light to generate ultrasound waves for USCT measurements was also proposed by Xia *et al.*[33]

3.4.1. *Passive element enriched PACT*

The passive element enriched PACT system utilized both ultrasound and PA measurements simultaneously

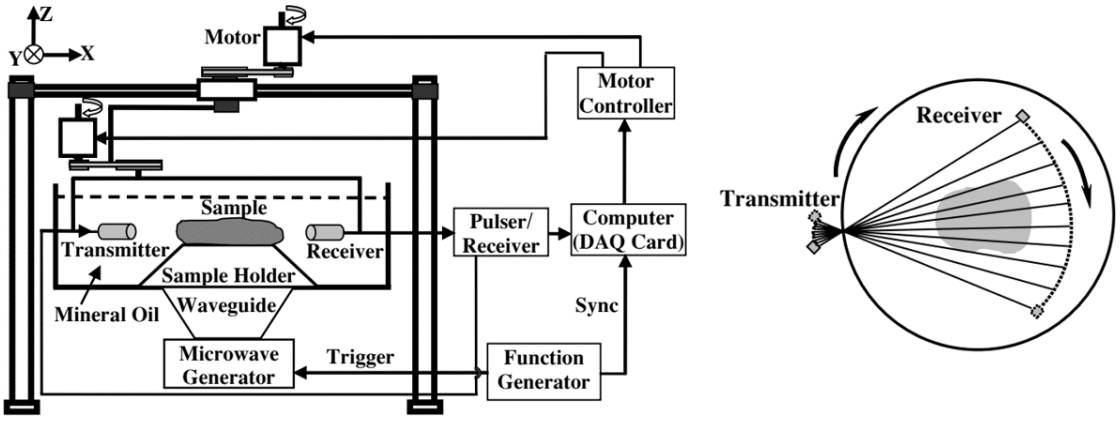

Fig. 9. Experimental set-up (a) and scanning geometry (b) of the combined USCT and thermoacoustic tomography system. Reproduced with permission from Ref. 31.

to get accurate SOS maps and used this information to reconstruct more accurate PA images.[22,66,67]

The imaging model illustrated in Eq. (4) shows that the generated pressure can be seen as the projections over iso-TOF contours determined in Eq. (5), which depends on the SOS distribution $v(\mathbf{r})$. In the case of homogeneous SOS distribution, the acoustic ray path is straight and the TOF is mainly decided by the SOS and travel distance. While in heterogeneous situations, the ray path is usually curved due to reflection effect as the wavefront passes through regions with different SOS. Given the SOS map estimated from USCT measurements, the high accuracy fast marching method that applies a second-order approximation is used to solve the eikonal equation.[68–70] Then, the ray path corresponding with the shortest arrival time can be traced and used to reconstruct PA images.

Figure 10 shows the schematic of passive elements enriched PACT system and reconstructed images of *ex vivo* experiments. The detector is a curvilinear array containing 32 elements and used as detectors for both USCT and PACT measurements. The system performs USCT and PACT measurements in sequence and uses the SOS map obtained in USCT to correct PA images. In the USCT process, a laser pulse was used to illuminant a strand of horsetail hair to generate ultrasound pulses as source signals. The incorporating of the SOS map into PA image reconstruction process improves image quality significantly.

3.4.2. *Concurrent optical absorption and SOS imaging*

Merčep and coworkers developed a transmission-reflection optoacoustic ultrasound (TROPUS) small animal imaging platform that combines both the PACT and the USCT with transmission and reflection modes.[34] The system can realize multi-modal imaging, including PA, SOS, acoustic reflectivity, acoustic attenuation imaging. The schematic of the TROPUS system is shown in Fig. 11. Small animals are surrounded by a ring transducer array consisting of 512 elements. The system could work in both receive-only and transmit-receive modes. In the receive-only mode, all elements are used to collect PA signals, while in the transmit-receive mode, all elements are activated to transmit ultrasound waves and receive the reflected and transmitted waves.

In vivo experimental results are shown in Fig. 12. The first column is the PA images. The second column of the images is constructed from the reflection mode, while the SOS (third column) and acoustic attenuation (fourth column) are constructed from transmission mode. The results of SOS images were segmented into two parts with different SOS. These images are then incorporated into PA reconstruction to enhance the image quality.

This imaging platform shows great potential for the combination of USCT and PACT setups. All the information that the system provides is associated because it relates to the characteristics of the

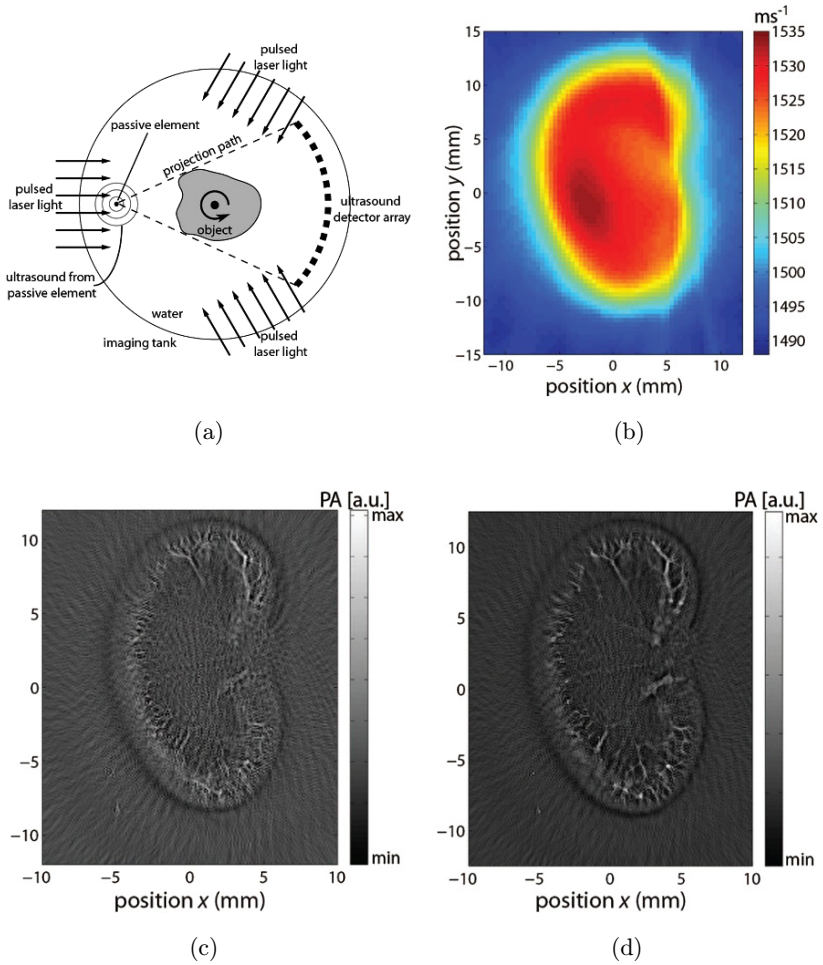

Fig. 10. Passive element enriched PACT. (a) Schematic. (b) SOS map reconstructed from the acquired passive-element measurement of the imaging area, (c) PA image reconstructed with a uniform SOS of 1540 m/s, (d) SOS compensated PA image using the SOS values from (a). Reproduced with permission from Ref. 22.

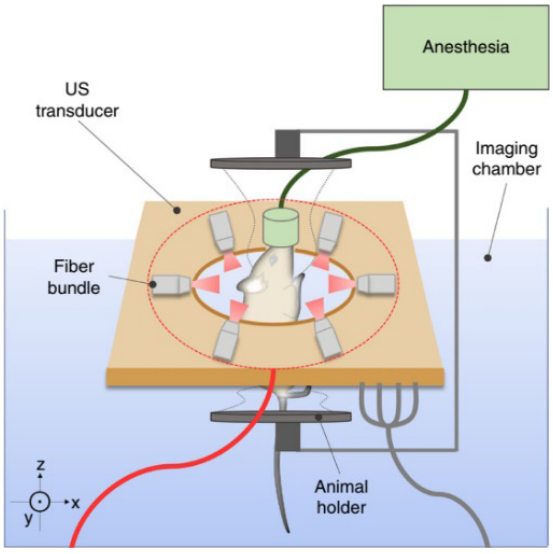

Fig. 11. Diagram of the USCT enhanced PACT imaging system. Reproduced with permission from Ref. 34.

same tissues. Results of one modality can be used to compensate for others, and different results can be combined to show more information.

4. Discussion and Conclusion

In summary, we reviewed four major types of approaches aiming to solve the acoustic heterogeneity problem in PACT. The half-time or partial-time approaches discard distorted measurement data in the time domain and recover PA images using conventional reconstruction algorithms with an empirically determined constant SOS. Since the data truncation step barely increases computational complexity, these approaches are simple and fast. In contrast, the autofocus approaches utilize full-time measurement data and an optimum SOS for image reconstruction. The optimum SOS is iteratively

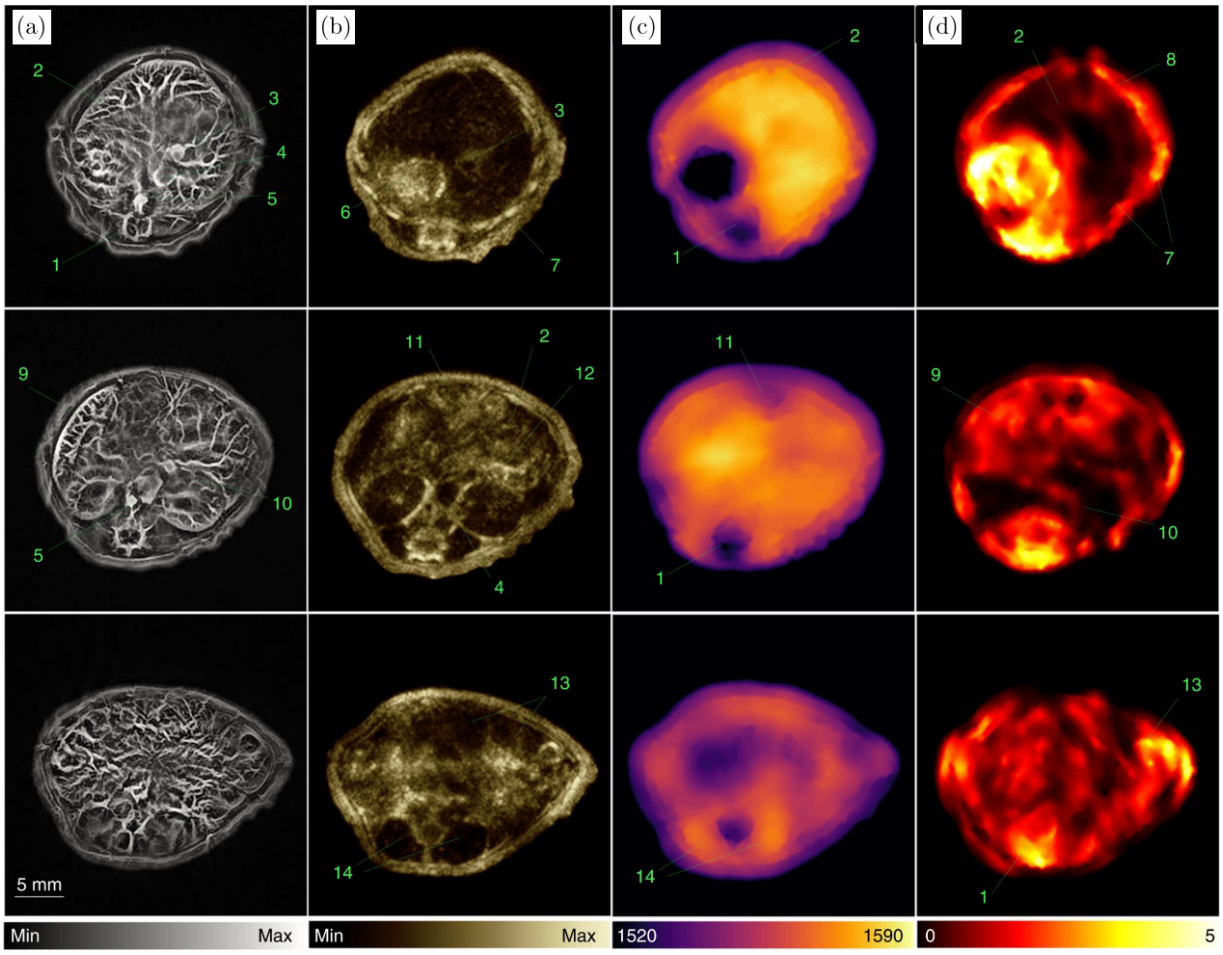

Fig. 12. USCT enhanced PACT imaging. (a) Three representative PA images of the cross-sections of a mouse. (b) Corresponding reflection-mode ultrasound images. (c) and (d) Corresponding transmission-mode ultrasound images showing the distribution of the SOS and acoustic attenuation, respectively. 1: spinal cord; 2: liver; 3: vena porta; 4: vena cava; 5: aorta; 6: stomach; 7: ribs; 8: skin/fat layer; 9: spleen; 10: right kidney; 11: cecum; 12: pancreas; 13: intestines; 14: muscle. Reproduced with permission from Ref. 34.

determined by evaluating a cost function describing the quality of the images or signals. Since this optimization procedure requires additional computing resources, the autofocus approaches have higher time and space complexities. Overall, the half-time/partial-time approaches and the autofocus approaches can only mitigate image artifacts and distortions to some extent in real scenarios because they are all based on the assumption that biological tissues have a constant SOS, which, however, is not true.

The joint reconstruction approaches and the USCT-enhanced approaches have improved performance in mitigating acoustic heterogeneity in PACT. The joint reconstruction approaches first segment the SOS map into multiple regions, each of which has a constant SOS, and then simultaneously recover the optical absorption map and the SOS map by optimizing a cost function using PACT measurement data alone. The joint reconstruction approaches are mathematically more complicated than the half-time and autofocus approaches and suffer from the problem of high complexity and numerical instability because the cost function may not be convex. However, this type of approach could still significantly improve image quality.[29,52] The USCT-enhanced reconstruction approaches first measure heterogeneous SOS maps by USCT and then incorporate the information into the image reconstruction model to improve image quality. The SOS model in USCT-enhanced approaches is experimentally obtained rather than based on simplified assumptions as in previous three approaches and, therefore, is more accurate. USCT-enhanced

Table 1. Performance comparison of the four approaches for acoustic heterogeneity mitigation.

Approaches	Complexity	Convex	Computational cost	Extra hardware requirement	Performance
Half-time/partial-time	Low	Yes	Low	No	Good
Autofocus	Moderate	Yes	Moderate	No	Good
Joint reconstruction	High	No.[30,52]	High	No	Excellent
USCT-enhanced	High	Yes	High	Yes	Excellent

reconstruction approaches are more stable but need extra setups to perform USCT measurements. Table 1 briefly summarizes the typical performance of the four approaches for acoustic heterogeneity migration in practical applications.

It should be noted that acoustic heterogeneity induced TOF errors in PACT measurements are distinct for different detection geometries. Some correction approaches are independent of measurement geometries while others are designed for special detector apertures. For example, the half-time or partial-time approaches,[23,24] joint reconstruction approaches,[28–30] and the USCT-enhanced approaches[31–34] were all developed based on ring or spherical detection geometries. Although the principles are generic and may be extended to other detection apertures, the image reconstruction process may become quite challenging. In addition, the autofocusing approaches[25–27] enhance image quality using an optimum SOS by evaluating a focusing function and has no restrictions on the detection geometries.

The choice of the approaches for the correction of acoustic heterogeneity should depend on experimental conditions. The half-time/partial-time approaches and the autofocusing approaches are simple and fast but have limited performance. The joint reconstruction approaches have improved performance but suffer from the problem of high complexity and numerical instability. The USCT-enhanced approaches have the highest performance but require extra hardware to perform USCT measurements, which is not feasible in some practical applications. For situations where USCT measurements are difficult, the joint reconstruction approaches provide a good alternative.

Acknowledgments

This work was supported in part by the National Natural Science Foundation of China (NSFC) under Grant No. 61705216, in part by the Major Science and Technology Project of Anhui Province under Grant No. 18030801138, in part by the Zhejiang Lab under Grant No. 2019MC0AB01, in part by the Research Funds of the Double First-Class Initiative, in part by the Research Fund of the USTC Smart City Institute, in part by the CAS Pioneer Hundred Talents Program, and in part by the Startup Fund of the University of Science and Technology of China (USTC).

Conflicts of Interest

The authors have no relevant conflicts of interest to disclose.

References

1. L. V. Wang, "Multiscale photoacoustic microscopy and computed tomography, *Nat. Photon.* **3**, 503 (2009).
2. L. V. Wang, J. Yao, "A practical guide to photoacoustic tomography in the life sciences," *Nat. Meth.* **13**, 627 (2016).
3. L. V. Wang, "Tutorial on photoacoustic microscopy and computed tomography," *IEEE J. Sel. Top. Quantum Electron.* **14**, 171 (2008).
4. C. Tian, M. Pei, K. Shen, S. Liu, Z. Hu, T. Feng, "Impact of system factors on the performance of photoacoustic tomography scanners," *Phys. Rev. Appl.* **13**, 014001 (2020).
5. L. Lin, P. Hu, J. Shi, C. M. Appleton, K. Maslov, L. Li, R. Zhang, L. V. Wang, "Single-breath-hold photoacoustic computed tomography of the breast," *Nat. Commun.* **9**, 2352 (2018).
6. G. P. Luke, S. Y. Emelianov, "Label-free detection of lymph node metastases with US-guided functional photoacoustic imaging," *Radiology* **277**, 435 (2015).
7. J. Jo, C. Tian, G. Xu, J. Sarazin, E. Schiopu, G. Gandikota, X. Wang, "Photoacoustic tomography for human musculoskeletal imaging and inflammatory arthritis detection," *Photoacoust.* **12**, 82 (2018).

8. S. Liu, H. Wang, C. Zhang, J. Dong, S. Liu, R. Xu, C. Tian, "In vivo photoacoustic sentinel lymph nodes imaging using clinically-approved carbon nanoparticles," *IEEE Trans. Biomed. Eng.* (2020).
9. H. Wang, S. Liu, T. Wang, C. Zhang, T. Feng, C. Tian, "Three-dimensional interventional photoacoustic imaging for biopsy needle guidance with a linear array transducer," *J. Biophoton.* **12**, e201900212 (2019).
10. C. Tian, W. Zhang, A. Mordovanakis, X. Wang, Y. M. Paulus, "Noninvasive chorioretinal imaging in living rabbits using integrated photoacoustic microscopy and optical coherence tomography," *Opt. Exp.* **25**, 15947 (2017).
11. C. Tian, W. Qian, X. Shao, Z. Xie, X. Cheng, S. Liu, Q. Cheng, B. Liu, X. Wang, "Plasmonic nanoparticles with quantitatively controlled bioconjugation for photoacoustic imaging of live cancer cells," *Adv. Sci.* **3**, 1600237 (2016).
12. C. Tian, Z. Xie, M. L. Fabiilli, X. Wang, "Imaging and sensing based on dual-pulse nonlinear photoacoustic contrast: A preliminary study on fatty liver," *Opt. Lett.* **40**, 2253 (2015).
13. M. Xu, L. V. Wang, "Universal back-projection algorithm for photoacoustic computed tomography," *Phys. Rev. E* **71**, 016706 (2005).
14. D. Finch, S. K. Patch, "Determining a function from its mean values over a family of spheres," *SIAM J. Math. Anal.* **35**, 1213 (2004).
15. L. A. Kunyansky, "Explicit inversion formulae for the spherical mean Radon transform," *Inverse Probl.* **23**, 373 (2007).
16. K. Wang, M. A. Anastasio, "A simple Fourier transform-based reconstruction formula for photoacoustic computed tomography with a circular or spherical measurement geometry," *Phys.Med. Biol.* **57**, N493 (2012).
17. C. Huang, A. A. Oraevsky, M. A. Anastasio, "Investigation of limited-view image reconstruction in optoacoustic tomography employing a priori structural information," *Image Reconstruction from Incomplete Data VI*, p. 780004, International Society for Optics and Photonics (2010).
18. C. Huang, L. Nie, R. W. Schoonover, Z. Guo, C. O. Schirra, M. A. Anastasio, L. V. Wang, "Aberration correction for transcranial photoacoustic tomography of primates employing adjunct image data," *J. Biomed. Opt.* **17**, 066016 (2012).
19. Y. Xu, L. V. Wang, "Effects of acoustic heterogeneity in breast thermoacoustic tomography," *IEEE Trans. Ultrason. Ferroelectr. Freq. Control* **50**, 1134 (2003).
20. X. L. Deán-Ben, V. Ntziachristos, D. Razansky, "Effects of small variations of speed of sound in optoacoustic tomographic imaging," *Med. Phys.* **41**, 073301 (2014).
21. J. Tick, A. Pulkkinen, T. Tarvainen, "Modelling of errors due to speed of sound variations in photoacoustic tomography using a Bayesian framework," *Biomed. Phys. Eng. Exp.* **6**, 015003 (2019).
22. J. Jose, R. G. Willemink, W. Steenbergen, C. H. Slump, T. G. van Leeuwen, S. Manohar, "Speed-of-sound compensated photoacoustic tomography for accurate imaging," *Med. Phys.* **39**, 7262 (2012).
23. M. A. Anastasio, J. Zhang, X. Pan, Y. Zou, G. Ku, L. V. Wang, "Half-time image reconstruction in thermoacoustic tomography," *IEEE Trans. Med. Imaging* **24**, 199 (2005).
24. J. Poudel, T. P. Matthews, L. Li, M. A. Anastasio, L. V. Wang, "Mitigation of artifacts due to isolated acoustic heterogeneities in photoacoustic computed tomography using a variable data truncation-based reconstruction method," *J. Biomed. Opt.* **22**, 041018 (2017).
25. B. E. Treeby, T. K. Varslot, E. Z. Zhang, J. G. Laufer, P. C. Beard, "Automatic sound speed selection in photoacoustic image reconstruction using an autofocus approach," *J. Biomed. Opt.* **16**, 090501 (2011).
26. C. Yoon, J. Kang, S. Han, Y. Yoo, T.-K. Song, J. H. Chang, "Enhancement of photoacoustic image quality by sound speed correction: ex vivo evaluation," *Opt. Exp.* **20**, 3082 (2012).
27. B. Cong, K. Kondo, T. Namita, M. Yamakawa, T. Shiina, "Photoacoustic image quality enhancement by estimating mean sound speed based on optimum focusing," *Jpn. J. Appl. Phys.* **54**, 07HC13 (2015).
28. J. Zhang, M. A. Anastasio, "Reconstruction of speed-of-sound and electromagnetic absorption distributions in photoacoustic tomography," *Photons Plus Ultrasound: Imaging and Sensing 2006: The Seventh Conf. Biomedical Thermoacoustics, Optoacoustics, and Acousto-optics*, p. 608619, International Society for Optics and Photonics (2006).
29. T. P. Matthews, J. Poudel, L. Li, L. V. Wang, M. A. Anastasio, "Parameterized joint reconstruction of the initial pressure and sound speed distributions for photoacoustic computed tomography," *SIAM J. Imaging Sci.* **11**, 1560 (2018).
30. C. Cai, X. Wang, K. Si, J. Qian, J. Luo, C. Ma, "Feature coupling photoacoustic computed tomography for joint reconstruction of initial pressure and sound speed in vivo," *Biomed. Opt. Exp.* **10**, 3447 (2019).
31. X. Jin and L. V. Wang, "Thermoacoustic tomography with correction for acoustic speed variations," *Phys. Med. Biol.* **51**, 6437 (2006).

32. S. Manohar, R. G. Willemink, F. van der Heijden, C. H. Slump, T. G. van Leeuwen, "Concomitant speed-of-sound tomography in photoacoustic imaging," *Appl. Phys. Lett.* **91**, 131911 (2007).
33. J. Xia, C. Huang, K. Maslov, M. A. Anastasio, L. V. Wang, "Enhancement of photoacoustic tomography by ultrasonic computed tomography based on optical excitation of elements of a full-ring transducer array," *Opt. Lett.* **38**, 3140 (2013).
34. E. Merčep, J. L. Herraiz, X. L. Deán-Ben, D. Razansky, "Transmission–reflection optoacoustic ultrasound (TROPUS) computed tomography of small animals," *Light. Sci. Appl.* **8**, 18 (2019).
35. S. Liu, Z. Zheng, X. Sun, Z. Zhao, Y. Zheng, H. Jiang, X. Zhu, Q. H. Liu, "Reducing acoustic inhomogeneity based on speed of sound autofocus in microwave induced thermoacoustic tomography," *IEEE Trans. Biomed. Eng.* (2019).
36. Y. Sun, S. Duthaler, B. J. Nelson, "Autofocusing in computer microscopy: Selecting the optimal focus algorithm," *Microsc. Res. Tech.* **65**, 139 (2004).
37. D. L. Marks, A. L. Oldenburg, J. J. Reynolds, S. A. Boppart, "Autofocus algorithm for dispersion correction in optical coherence tomography," *Appl. Opt.* **42**, 3038 (2003).
38. A. Kingston, A. Sakellariou, A. Sheppard, T. Varslot, S. Latham, "An auto-focus method for generating sharp 3D tomographic images", *Developments in X-Ray Tomography VII*, p. 78040J, International Society for Optics and Photonics (2010).
39. S. Mandal, E. Nasonova, X. L. Deán-Ben, D. Razansky, "Optimal self-calibration of tomographic reconstruction parameters in whole-body small animal optoacoustic imaging," *Photoacoust.* **2**, 128 (2014).
40. A. Kirsch, O. Scherzer, "Simultaneous reconstructions of absorption density and wave speed with photoacoustic measurements," *SIAM J. Appl. Math.* **72**, 1508 (2012).
41. H. Liu, G. Uhlmann, "Determining both sound speed and internal source in thermo-and photoacoustic tomography," *Inverse Probl.* **31**, 105005 (2015).
42. H. Jiang, Z. Yuan, X. Gu, "Spatially varying optical and acoustic property reconstruction using finite-element-based photoacoustic tomography," *JOSA A* **23**, 878 (2006).
43. Z. Yuan, Q. Zhang, H. Jiang, "Simultaneous reconstruction of acoustic and optical properties of heterogeneous media by quantitative photoacoustic tomography," *Opt. Exp.* **14**, 6749 (2006).
44. Z. Yuan, H. Jiang, "Three-dimensional finite-element-based photoacoustic tomography: Reconstruction algorithm and simulations," *Med. Phys.* **34**, 538 (2007).
45. G. Chen, X. Wang, J. Wang, Z. Zhao, Z.-P. Nie, Q. H. Liu, "Tr adjoint imaging method for mitat," *Prog. Electromagn. Res.* **46**, 41 (2013).
46. T. Ding, K. Ren, S. Vallélian, "A one-step reconstruction algorithm for quantitative photoacoustic imaging," *Inverse Probl.* **31**, 095005 (2015).
47. C. Huang, K. Wang, L. Nie, L. V. Wang, M. A. Anastasio, "Full-wave iterative image reconstruction in photoacoustic tomography with acoustically inhomogeneous media," *IEEE Trans. Med. Imaging* **32**, 1097 (2013).
48. C. Bunks, F. M. Saleck, S. Zaleski, G. Chavent, "Multiscale seismic waveform inversion," *Geophysics* **60**, 1457 (1995).
49. S. J. Norton, "Iterative inverse scattering algorithms: Methods of computing Frechet derivatives," *J. Acoust. Soc. Am.* **106**, 2653 (1999).
50. X. Pan, Y. Zou, M. A. Anastasio, "Data redundancy and reduced-scan reconstruction in reflectivity tomography," *IEEE Trans. Image Process* **12**, 784 (2003).
51. H. Shan, G. Wang, Y. Yang, "Simultaneous reconstruction of the initial pressure and sound speed in photoacoustic tomography using a deep-learning approach", *Novel Optical Systems, Methods, and Applications XXII*, p. 1110504, International Society for Optics and Photonics (2019).
52. C. Huang, K. Wang, R. W. Schoonover, L. V. Wang, M. A. Anastasio, "Joint reconstruction of absorbed optical energy density and sound speed distributions in photoacoustic computed tomography: a numerical investigation," *IEEE Trans. Comput. Imaging* **2**, 136 (2016).
53. P. Stefanov, G. Uhlmann, "Instability of the linearized problem in multiwave tomography of recovery both the source and the speed," *Inverse Probl. Imag.* **7**, 1367 (2013).
54. K. S. Hickmann, "Unique determination of acoustic properties from thermoacoustic data" (2010).
55. T. P. Matthews, M. A. Anastasio, "Joint reconstruction of the sound speed and initial pressure distributions for ultrasound computed tomography and photoacoustic computed tomography," in *Medical Imaging 2017: Ultrasonic Imaging and Tomography*, p. 101390B, International Society for Optics and Photonics (2017).
56. Y. Hristova, P. Kuchment, L. Nguyen, "Reconstruction and time reversal in thermoacoustic tomography in acoustically homogeneous and inhomogeneous media," *Inverse Probl.* **24**, 055006 (2008).
57. Y. Xu, L. V. Wang, "Time reversal and its application to tomography with diffracting sources," *Phys. Rev. Lett.* **92**, 033902 (2004).
58. B. E. Treeby, E. Z. Zhang, B. T. Cox, "Photoacoustic tomography in absorbing acoustic

media using time reversal," *Inverse Probl.* **26**, 115003 (2010).
59. S. R. Arridge, M. M. Betcke, B. T. Cox, F. Lucka, B. E. Treeby, "On the adjoint operator in photoacoustic tomography," *Inverse Probl.* **32**, 115012 (2016).
60. J. Qian, P. Stefanov, G. Uhlmann, H. Zhao, "An efficient Neumann series–based algorithm for thermoacoustic and photoacoustic tomography with variable sound speed," *SIAM J. Imaging Sci.* **4**, 850 (2011).
61. P. Stefanov, G. Uhlmann, "Thermoacoustic tomography with variable sound speed," *Inverse Probl.* **25**, 075011 (2009).
62. D. Modgil, M. A. Anastasio, P. J. La Rivière, "Image reconstruction in photoacoustic tomography with variable speed of sound using a higher-order geometrical acoustics approximation," *J. Biomed. Opt.* **15**, 021308 (2010).
63. M. A. Anastasio, J. Zhang, X. Pan, "Image reconstruction in thermoacoustic tomography with compensation for acoustic heterogeneities," *Medical Imaging 2005: Ultrasonic Imaging and Signal Processing*, p. 298, International Society for Optics and Photonics (2005).
64. X. L. Deán-Ben, V. Ntziachristos, D. Razansky, "Statistical optoacoustic image reconstruction using a-priori knowledge on the location of acoustic distortions," *Appl. Phys. Lett.* **98**, 171110 (2011).
65. C. Zhang, Y. Wang, "A reconstruction algorithm for thermoacoustic tomography with compensation for acoustic speed heterogeneity," *Phys. Med. Biol.* **53**, 4971 (2008).
66. R. G. Willemink, S. Manohar, J. Jose, K. Slump, F. van der Heijden, T. G. van Leeuwen, "Simultaneous imaging of ultrasound attenuation, speed of sound, and optical absorption in a photoacoustic setup," in *Medical Imaging 2009: Ultrasonic Imaging and Signal Processing*, p. 72650J, International Society for Optics and Photonics (2009).
67. J. Jose, R. G. Willemink, S. Resink, D. Piras, J. G. van Hespen, C. H. Slump, W. Steenbergen, T. G. van Leeuwen, S. Manohar, "Passive element enriched photoacoustic computed tomography (PER PACT) for simultaneous imaging of acoustic propagation properties and light absorption," *Opt. Exp.* **19**, 2093 (2011).
68. S. Li, K. Mueller, M. Jackowski, D. P. Dione, L. H. Staib, "Fast marching method to correct for refraction in ultrasound computed tomography," *3rd IEEE Int. Symp. Biomedical Imaging: Nano to Macro*, p. 896 IEEE (2006).
69. S. Li, K. Mueller, M. Jackowski, D. Dione, L. Staib, "Physical-space refraction-corrected transmission ultrasound computed tomography made computationally practical," *Int. Conf. Medical Image Computing and Computer-Assisted Intervention*, p. 280, Springer (2008).
70. M. Heijblom, D. Piras, W. Xia, J. C. van Hespen, J. Klaase, F. Van den Engh, T. Van Leeuwen, W. Steenbergen, S. Manohar, "Visualizing breast cancer using the Twente photoacoustic mammoscope: What do we learn from twelve new patient measurements?," *Opt. Exp.* **20**, 11582 (2012).